Numerical Simulations of the Ram Pressure-Driven Rayleigh-Taylor Instability

Maggie Hilderbran

April 2, 2019

Abstract

Star formation in the Galactic disk is fueled by continuous accretion of gas from the Galactic halo. This infalling gas is usually identified in the form of high-velocity clouds (HVCs), so named because their velocities do not match a standard Galactic rotation pattern. As they pass through the halo, HVCs are disrupted by a series of fluid instabilities. The Rayleigh-Taylor instability (RTI), driven by ram pressure, occurs at the interface between the cold, dense cloud and the hot, diffuse halo. I perform a systematic investigation of the RTI under conditions relevant to HVCs in the halo, exploring how the instability contributes to the breakup of these clouds. I use the grid-based fluid dynamics code Athena (Stone et al. 2008) to solve the equations of ideal magnetohydrodynamics, simulating the instability at the halo-cloud interface. Step-by-step addition of radiative processes and magnetic fields provides an understanding of their effects on the evolution of the RTI. Cooling causes rapid fragmentation of the interface and dampens the instability, in line with Vietri et al. (1997). The addition of a uniform magnetic field suppresses the instability in two dimensions but not in three dimensions, consistent with Stone & Gardiner (2007). In contrast, tangled magnetic fields, which may be a more realistic model, produce results more like the hydrodynamical case. Because the plane-parallel geometry I assume does not take into account mass flow around (and away from) the interface, the instability growth found in my models is likely an upper limit compared to more realistic situations.

1 Introduction

Star formation in the Galactic disk is fueled by continuous accretion of gas from the Galactic halo. This infalling gas is usually identified in the form of high-velocity clouds (HVCs), so named because their velocities are inconsistent with a standard Galactic rotation pattern. HVCs are typically defined as having speeds differing from the local standard of rest by at least 90 $\mathrm{km\,s^{-1}}$ (Wakker & van Woerden 1997).

Yet despite their significance for Galactic evolution, the origin of HVCs remains uncertain. Wakker & van Woerden (1997) argued that given the observed diversity of these clouds, multiple origin hypotheses should be considered: one for the Magellanic Stream, another for clouds in the "Outer Arm Extension," and one or more for other HVCs. The fountain model and accretion from dwarf galaxies and/or the intergalactic medium are among the central theories. In the fountain model, Shapiro & Field (1976) proposed that hot ($T \sim 10^6$ K) gas in the interstellar medium (ISM) rises into the Galactic halo, where it cools through radiation and condenses into clouds that fall back to the disk at high velocities (see also Bregman 1980). Alternatively, HVCs may be the result of accretion of intergalactic gas, either remaining from the formation of our galaxy (Oort 1966, 1970) or pulled from satellite galaxies (e.g., the Magellanic Clouds) via tidal forces or ram pressure stripping (Wakker & van Woerden 1997). These hypotheses are not mutually exclusive: in a more recent numerical investigation of the HVC complex C, Fraternali et al. (2015) brought together the fountain and accretion models, demonstrating that both ejection of hot gas from the galactic disk and accretion of external gas could explain the formation of the cloud.

Determining distances to HVCs plays a critical role in the assessment of these possible origin scenarios. Constraints on distance can be acquired from absorption lines (e.g., Wakker 2001; Wakker et al. 2007, 2008; Thom et al. 2006, 2008; Richter et al. 2015), yet due to the difficulty of identifying appropriate background sources, few clouds have these constraints. Distance can be also be determined via the association of clouds with known complexes (e.g., Saul et al. 2012). Alternatively, cloud metallicities can be used to evaluate origin scenarios; however, mixing with and accretion of ambient halo material present challenges for interpreting the measurements.

Related to the question of cloud origin is that of cloud survival. During their passage through the Galactic halo, HVCs interact with the ambient gas through a series of fluid instabilities. Simulation results have consistently suggested that under conditions typical for HVCs, the clouds should be disrupted quickly enough to raise the question of why we actually observe so many of them. For example, Quilis & Moore (2001) and Heitsch & Putman (2009) both show that typical HVCs would not survive passage through the halo to make it to the Galactic disk. While Forbes & Lin (2018) implicitly suggest that the usual numerical experiments are over-idealized by omitting a warm envelope around the cold cloud, here, I take a closer look at one of the fluid instabilities supposed to drive the disruption of HVCs.

The Rayleigh-Taylor instability (RTI), driven by ram pressure, occurs at the interface between the cold, dense cloud and the hot, diffuse Galactic halo. I perform a systematic investigation of this instability, beginning with minimal assumptions about the physical processes, then adding step-by-step the physics relevant to the regime in which HVCs are found. I use the grid-based fluid dynamics code Athena (Stone et al. 2008) to solve the equations of ideal magnetohydrodydnamics (MHD), simulating the instability and its growth at the halo-cloud interface.

1.1 The Rayleigh-Taylor Instability

The RTI occurs when a denser fluid is accelerated against a less dense fluid (Figure 1). Perturbation of the interface between the two fluids results in growth of the instability and mixing of the fluids.

The physical processes underlying the instability are best understood through the gravity-driven RTI. Figure 1a shows the initial conditions for the gravity-driven RTI, where ρ_2 is the density of the heavier fluid and ρ_1 is the density of the lighter fluid, and $\vec{F}_G$ is the gravitational force given by the gravitational acceleration $\vec{g}$, which acts downwards. The interface between the two fluids is unstable, since it is energetically less favorable to have the heavier fluid at a higher gravitational potential energy than the lighter fluid. Thus, when the interface is perturbed, the instability will grow and the fluids will begin to mix, eventually switching places as the denser fluid falls down below the less dense fluid.

Alternatively, ram pressure, rather than gravity, can drive the RTI. Figure 1b shows the ram pressure-driven instability in the context of high-velocity clouds, where a dense cloud of gas moves through the diffuse Galactic halo. The densities ρ_c and ρ_h denote the cloud and halo gas, respectively, and $\vec{v}_h$ is the velocity of the halo gas relative to the interface. The ram pressure from the inflow of halo gas drives the instability.

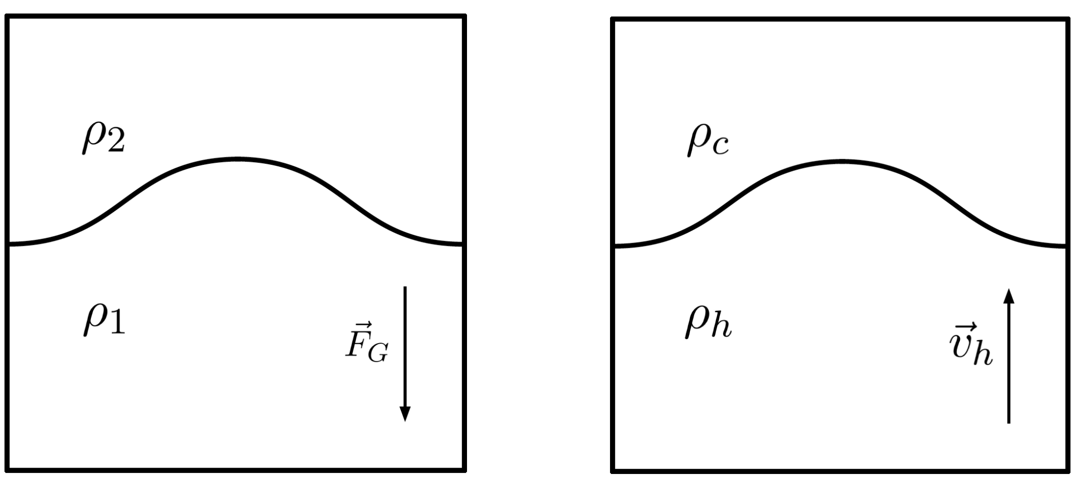

(a) The classical, gravity-driven instability.

(b) The ram pressure-driven instability.

Figure 1: Two models for the RTI.

A detailed stability analysis of the gravity-driven RTI for an ideal gas including surface tension has been given by Chandrasekhar (1961). For two fluids separated by a horizontal interface at $z = 0$, with densities ρ_1

below the interface and ρ_2 above, perturbations to the density ρ, pressure P, and velocity v at the interface can result in instability. For the RTI, P and ρ depend only upon z.

The hydrodynamical evolution of a fluid in an Eulerian reference frame can be written in the form of conservation laws. Mass conservation is described by

$$\partial_t \rho + \nabla(\rho v) = 0, \tag{1}$$

where ρ is the density and v is the vector-valued velocity of the fluid, and momentum conservation can be expressed as

$$\partial_t(\rho v) + \nabla(\rho v v) = -\nabla P - \rho g_z \tag{2}$$

where P is the pressure of the fluid. Here, the fluid is assumed to be inviscid. Linear perturbations are introduced into the quantities ρ, P, and v:

$$\rho = \rho_0 + \delta\rho \tag{3}$$

$$P = P_0 + \delta P \tag{4}$$

$$v = \delta v, \tag{5}$$

where the perturbation of v is simply δv because v_0 is defined to be zero (the interface is at rest). For discontinuities in density at some positions z_s (for $s = 1$, 2, 3, etc.), the interface position is then

$$z_s + \delta z_s(x, y, t). \tag{6}$$

Applying Equations 1 and 2 to the perturbations, the condition for mass conservation (along the z-direction) becomes

$$\partial_t \delta\rho + v_z \partial_z \rho_0 = 0. \tag{7}$$

Momentum conservation yields

$$\rho_0 \partial_t v_x = -\partial_x \delta P \tag{8}$$

$$\rho_0 \partial_t v_y = -\partial_y \delta P \tag{9}$$

$$\rho_0 \partial_t v_z = -\partial_z \delta P - g\delta\rho + \sum_s \left[T_s \left(\frac{\partial^2}{\partial x^2} + \frac{\partial^2}{\partial y^2} \right) \delta z_s \right] \delta(z - z_s), \tag{10}$$

where T_s is the surface tension. The last term in Equation 10 comes from the discontinuity in the normal stresses as required for equilibrium,

$$T_s \left(\frac{\partial^2}{\partial x^2} + \frac{\partial^2}{\partial y^2} \right) \delta z_s. \tag{11}$$

The fluid is taken to be incompressible (such that $\nabla \cdot v = 0$):

$$\partial_x v_x + \partial_y v_y + \partial_z v_z = 0. \tag{12}$$

We look for solutions for δP, $\delta\rho$, and v dependent upon x, y, and t in the form $\exp(ik_x x + ik_y y + nt)$, where k_x and k_y are the wavenumbers for modes in the x- and y-directions, respectively, and n is the frequency or growth rate. If P, ρ, and v are dependent upon x, y, and t in this manner, then Equations 7- 10 and 12 become

$$n\delta\rho = -v_z \partial_z \rho_0, \tag{13}$$

$$n\rho_0 v_x = -ik_x \delta P \tag{14}$$

$$n\rho_0 v_y = -ik_y \delta P \tag{15}$$

$$n\rho_0 v_z = -\partial_z \delta P - g\delta\rho - k^2 \sum_s (T_s \delta z_s)\, \delta(z - z_s) \tag{16}$$

$$ik_x v_x + ik_y v_y = -\partial_z v_z \tag{17}$$

where $k = \sqrt{k_x^2 + k_y^2}$.

Equations 14, 15, and 17 can be solved together to obtain

$$k^2 \delta P = -n\rho_0 \left(\frac{d}{dz} v_z \right), \tag{18}$$

while combination of Equations 13 and 16 yields

$$\frac{d}{dz}\delta P = -n\rho_0 v_z + \frac{g}{n} \left(\frac{d}{dz}\rho_0 \right) v_z - \frac{k^2}{n} \sum_s \left(T_s v_{z,s} \right) \delta(z - z_s), \tag{19}$$

where δz_s has been replaced by $v_{z,s}/n$.

By eliminating δP from Equations 18 and 19, the following governing equation is obtained:

$$\frac{d}{dz}\left[\rho_0 \left(\frac{d}{dz} v_z \right) \right] = k^2 \left[\left(-\frac{g}{n^2} \left(\frac{d}{dz}\rho_0 \right) + \frac{k^2}{n^2} \sum_s T_s \delta(z - z_s) \right) v_z + \rho_0 v_z \right]. \tag{20}$$

For $z \neq z_s$, the surface tension terms in these equations disappear. However, at the interface between the two fluids, integration of Equation 18 over a infinitesimal length around z_s gives

$$k^2 \Delta_s(\delta P) = \Delta_s \left[-n\rho_0 \left(\frac{d}{dz} v_z \right) \right], \tag{21}$$

where $\Delta_s(f) = f(z_s + 0) - f(z_s - 0)$ represents the jump in a quantity f across the interface at z_s. For Equation 19, integration across the surface yields

$$\Delta_s(\delta P) = \frac{g}{n} v_{z,s} \Delta_s(\rho_0) - \frac{k^2}{n} T_s v_{z,s}. \tag{22}$$

Combining Equations 21 and 22 results in the following jump condition for the interface between the fluids:

$$\Delta_s \left[\rho_0 \left(\frac{d}{dz} v_z \right) \right] = -\frac{k^2}{n^2} \left[g\Delta_s(\rho_0) - k^2 T_s \right] v_{z,s}. \tag{23}$$

Equation 20 is true for all positions except $z = z_s$, where Equation 23 is the governing equation. Setting $v_z = 0$ on the boundaries, the conditions from Equations 20 and 23 can be applied to obtain a dispersion relation for n.

For two fluids of uniform densities separated by a horizontal boundary at $z = 0$, n is given by

$$n^2 = gk \left(\frac{\rho_2 - \rho_1}{\rho_2 + \rho_1} - \frac{k^2 T}{g(\rho_2 + \rho_1)} \right), \tag{24}$$

where T is the surface tension (Chandrasekhar 1961). Instability occurs when n is real (that is, when $\rho_2 > \rho_1$). For configurations with $\rho_1 > \rho_2$, n is imaginary and stability is achieved.

If there is no surface tension ($T = 0$), the system is unconditionally unstable, and the growth of the perturbation amplitude due to the growth rate n is

$$\exp(nt) = \exp\left(t\sqrt{gk\mathcal{A}} \right), \tag{25}$$

with the Atwood number $\mathcal{A}$

$$\frac{\rho_2 - \rho_1}{\rho_2 + \rho_1}. \tag{26}$$

The above reasoning applies to not only the gravity-driven RTI but also the ram pressure-driven instability, in which the acceleration of the heavier fluid against the lighter one is caused by ram pressure rather than by gravity. As dense gas moves in a diffuse medium, the relative velocity v of the diffuse gas results in ram pressure

$$P_{\text{ram}} = \rho v^2. \tag{27}$$

In the case of a dense cloud (ρ_c) moving through diffuse gas (ρ_h), as shown in Figure 1b, this ram pressure corresponds to a drag force F_D, which causes an acceleration a_D:

$$a_D = \frac{F_D}{M_{\rm cloud}} = \frac{1}{2} c_w \frac{P_{\rm ram}}{\Sigma_{\rm cloud}}, \tag{28}$$

where $M_{\rm cloud}$ is the cloud mass, c_w is the drag coefficient, and $\Sigma_{\rm cloud}$ is the mean column density of the cloud (Roediger & Hensler 2008). In the ram pressure-driven instability, this acceleration from the drag force acts like the gravitational acceleration in the gravity-driven RTI.

In my idealized simulation setup, the expression for the acceleration due to ram pressure simplifies further due to the assumption of a plane-parallel geometry—instead of exploring the whole cloud, I focus on the leading surface interacting with the ambient gas. For this specific case,

$$a_D = \frac{\rho v^2}{\Sigma}, \tag{29}$$

where Σ is the surface density of the denser gas and ρv^2 is the ram pressure exerted on the dense gas by the diffuse gas.

1.2 The Effects of Heating and Cooling

To accurately model the evolution of the RTI at the edge of a high-velocity cloud in the Galactic halo, I include the effects of heating and radiative cooling processes that occur in interstellar gas.

For the RTI, the reasoning behind the effects of radiative losses parallels that given by Vietri et al. (1997) for the Kelvin-Helmholtz instability. When the cooling timescale in a region is shorter than the dynamical (sound crossing) time, the instability cannot propagate and therefore should remain relatively contained near the interface. Their numerical simulations indeed show confinement of the instability, as well as that turbulence at the cloud's edges generally does not easily reach the rest of the cloud (Vietri et al. 1997).

I anticipate similar conditions for the RTI: radiative losses due to cooling should create a damping effect, reducing the instability's growth and resulting in a more compressed, fragmented interface between the halo and cloud gas. The cooling gas may act as a mass sink as well, causing accretion.

Interstellar gas is heated and cooled through a wide array of physical processes (e.g., Dalgarno & McCray 1972), effectively leading to two or three coexisting regimes of density-temperature pairs, or "phases," that are in approximate pressure equilibrium (McKee & Ostriker 1977). Calculations by Wolfire et al. (1995) of the ISM thermal equilibrium temperature show this two-phase structure: the warm neutral medium (WNM) and the cold neutral medium (CNM) exist in pressure equilibrium, both with thermal pressures $P/k_B \simeq 10^3\text{-}10^4\,\mathrm{K\,cm^{-3}}$ (Wolfire et al. 1995).

Koyama & Inutsuka (2000) provided more accurate calculations of the equilibrium temperature by additionally accounting for the effects of the formation and cooling of H_2 and CO. The following heating processes are included in their calculations: photoelectric heating from small grains and polycyclic aromatic hydrocarbons, ionization heating by cosmic rays and x-rays, and heating from the formation and dissociation of H_2. For cooling, they account for atomic lines (Lyα, C II, O I, Fe II, and Si II), H_2 and CO ro-vibrational lines, and collisions of atoms and molecules with grains.

Koyama & Inutsuka (2002) provide a compact fit expression to the energy change rate

$$\dot{E} = n\Gamma - n^2\Lambda, \tag{30}$$

where n is the gas number density. I use their heating and cooling functions in my model. The cooling rate Λ, with typographical corrections given by Vázquez-Semadeni et al. (2007), is

$$\frac{\Lambda(T)}{\Gamma} = 10^7 \exp\left(\frac{-1.184\times10^5}{T+1000}\right) + 1.4\times10^{-2}\sqrt{T}\exp\left(\frac{-92}{T}\right)\ \mathrm{cm}^3, \tag{31}$$

where T is given in Kelvin. The two cooling processes dominating the radiative losses are Lyα and [C II] emission.

The heating rate Γ is

$$\Gamma = 2.0\times10^{-26}\,\mathrm{erg\,s^{-1}}. \tag{32}$$

The model of heating and cooling given by Wolfire et al. (1995) reflects a stable, two-phase interstellar medium. I set the initial density conditions of my model (Sec. 2.2.1) to be consistent with these phases, such that the halo and cloud gas are in thermal equilibrium and the pressure is constant across the simulation domain.

1.3 The Effects of Magnetic Fields

Chandrasekhar (1961) also analyzed the RTI in the case of magnetic fields both perpendicular to and parallel to the interface between the fluids.

A field $\vec{B}$ parallel to the interface produces an effective surface tension

$$T_{\text{eff}} = \frac{B^2}{2\pi k}\cos^2\theta, \tag{33}$$

where θ is the angle between the wavevector $\vec{k} = (k_x, k_y)$ and the magnetic field $\vec{B}$ (Chandrasekhar 1961). Modes perpendicular to $\vec{B}$ have an effective surface tension $T_{\text{eff}} = 0$. The magnetic field, therefore, has no impact on the growth of these modes.

For modes parallel to $\vec{B}$ (having a non-zero T_{eff}), the condition for real n given by Equation 24 is

$$\frac{\rho_2 - \rho_1}{\rho_2 + \rho_1} > \frac{k^2 T_{\text{eff}}}{g(\rho_2 + \rho_1)}, \tag{34}$$

yielding a critical wavenumber

$$k_c^2 = \frac{2\pi g k(\rho_2 - \rho_1)}{B^2}. \tag{35}$$

Above this critical wavenumber, the instability will be suppressed for modes parallel to $\vec{B}$. This wavenumber corresponds to a critical wavelength

$$\lambda_c = \frac{2\pi}{k_c} = \frac{B^2}{g(\rho_2 - \rho_1)}. \tag{36}$$

For $\lambda < \lambda_c$, n is imaginary, yielding oscillatory but stable solutions. For $\lambda > \lambda_c$, the instability will grow.

The critical field strength for an interface of length L is therefore

$$B_c = \sqrt{Lg(\rho_2 - \rho_1)}. \tag{37}$$

At field strengths $B > B_c$, the instability will be suppressed; B must be be smaller than B_c for growth to occur.

2 Method

To study the RTI evolution in the context of high-velocity clouds, I simulate a ram pressure-driven instability. I focus on the interface at which the instability occurs, rather than modeling the HVC in its entirety. The HVC is represented by the dense gas, and the galactic halo is represented by an inflow of diffuse gas, creating ram pressure that accelerates the dense cloud gas. I apply a perturbation to the halo-cloud interface and study the evolution of the resulting RTI.

2.1 Athena

I use the grid-based fluid dynamics code Athena (Stone et al. 2008) to solve the equations of ideal magnetohydrodynamics. Athena uses a fixed, cartesian grid, and I explore the instability in two and three dimensions.

2.1.1 Equations Solved

As given by Stone et al. (2008), Athena solves the following equations of ideal MHD:

$$\frac{\partial \rho}{\partial t} + \nabla \cdot (\rho \boldsymbol{v}) = 0, \tag{38}$$

$$\frac{\partial \rho \boldsymbol{v}}{\partial t} + \nabla \cdot (\rho \boldsymbol{v}\boldsymbol{v} - \boldsymbol{B}\boldsymbol{B} + \mathbf{P}^{*}) = 0, \tag{39}$$

$$\frac{\partial E}{\partial t} + \nabla \cdot [(E + P^{*})\, \boldsymbol{v} - \boldsymbol{B}\,(\boldsymbol{B} \cdot \boldsymbol{v})] = 0, \tag{40}$$

$$\frac{\partial \boldsymbol{B}}{\partial t} - \nabla \times (\boldsymbol{v} \times \boldsymbol{B}) = 0, \tag{41}$$

where the diagonal tensor $\mathbf{P}^{*}$ has components $P^{*} = P + B^2/2$ and the total energy density E is

$$E = \frac{P}{\gamma - 1} + \frac{1}{2}\rho v^2 + \frac{B^2}{2}, \tag{42}$$

with $B^2 = \boldsymbol{B} \cdot \boldsymbol{B}$ (Stone et al. 2008). The magnetic permeability μ is equal to 1 in the units of these equations. To obtain Equation 42, Athena uses an equation of state for an ideal gas, given by

$$P = (\gamma - 1)e, \tag{43}$$

where γ is the specific heat ratio and e is the internal energy density (Stone et al. 2008). I use $\gamma = 5/3$, corresponding to a monatomic gas.

2.1.2 Units

Athena performs calculations in its own system of computational units, which defines the following constants:

- $G = 1$, $[G] = \mathrm{cm}^3\ \mathrm{g}^{-1}\ \mathrm{s}^{-2}$
- $k_b = 1$, $[k_b] = \mathrm{erg}\ \mathrm{K}^{-1}$

Quantities in Athena's computational unit system can be converted to physical units:

$$q_{\mathrm{phys}} = q_0 \cdot q_{\mathrm{cu}}, \tag{44}$$

where q_{phys} is the quantity measured in physical units, q_0 is the conversion factor, and q_{cu} is the quantity in computational units.

The conversion factors used for conversion from computational to CGS units are given in Table 1. When applicable, the conversion factors are also provided in more relevant units.

2.1.3 Comoving Frame

To keep the interface between the dense and diffuse gas within the simulation domain, I use a comoving frame of reference that shifts to follow the interface, which is pushed in the $+y$ (three dimensions: $+z$) direction by ram pressure from the inflow of diffuse halo gas.

I track the interface via a scalar field S_0. The interface velocity v_{int} is then the center-of-mass upwards velocity:

$$v_{\mathrm{int}} = \frac{\sum_{i,j} v_y[i,j] \cdot S_0[i,j]}{\sum_{i,j} S_0[i,j]}. \tag{45}$$

From the interface velocity v_{int} I determine a velocity correction Δv, which increases with the distance between the interface and its intended central position:

$$\Delta v = v_{\mathrm{int}} \left(\frac{|y_{\mathrm{COM}}|}{0.3 l_y} \right), \tag{46}$$

quantity	conversion factor	CGS value	equivalent value
density	n_0	$1\ \mathrm{cm}^{-3}$	
temperature	T_0	1 K	
time	t_0	3×10^{15} s	95 Myr
length/position	l_0	2.724×10^{19} cm	8.83 pc
velocity	v_0	$9094\ \mathrm{cm\ s}^{-1}$	$0.091\,\mathrm{km\,s}^{-1}$
pressure	P_0	$1.381 \times 10^{-16}\ \mathrm{g\ cm}^{-1}\ \mathrm{s}^{-2}$ [Ba]	$1\,\mathrm{K\,cm}^{-3}$ (P_0/k_B)
energy	E_0	$2.79 \times 10^{42}\ \mathrm{g\ cm}^2\ \mathrm{s}^{-2}$ [erg]	2.79×10^{35} J
magnetic field	B_0	1.17×10^{-8} G	0.0117 µG

Table 1: Factors for conversion from computational to physical units.

where y_{COM} is the center-of-mass y-position

$$y_{\mathrm{COM}} = \frac{\sum_{i,j} y[i,j] \cdot S_0[i,j]}{\sum_{i,j} S_0[i,j]}. \tag{47}$$

In three dimensions, Δv is determined from v_z and z_{COM}.

The velocity correction Δv is then subtracted from the whole simulation grid, while simultaneously updating the vertical grid position. Thus, the grid moves with the interface, keeping the interface centered. Corrections are made accordingly to other variables (position, energy, etc.) to account for the velocity change. The upper and lower boundaries are updated with the velocity correction Δv for the comoving frame as well.

2.2 Simulation Parameters

The simulation domain is of size $L \times 2L$ (three dimensions: $L \times L \times 2L$), with $L = 1.0 = 8.8$ pc.

2.2.1 Initial Conditions

In two dimensions, the interface between the dense gas (representing the cloud) and the diffuse gas (representing the halo) is parallel to the x-axis. In the case of a standard sinusoidal perturbation at the halo-cloud interface, the perturbation shape is given by

$$y(x) = \cos\left(\frac{2\pi x}{l_x}\right), \tag{48}$$

where l_x is the length of the simulation domain along the x-axis. To model a random interface, the perturbation of the interface is determined by a sum of sinusoidal functions with random phase shifts, such that

$$y(x) = \sum_{k=1}^{k_{\max}} k^{-a} \cos\left(\frac{2\pi}{l_x}(kx + \phi)\right), \tag{49}$$

where $k_{\max} = 5$, $a = 1.5$, and ϕ is a random number chosen from the uniform distribution $U(0, 1)$.

The three-dimensional random interface is given by

$$z(x, y) = \sum_{k_x, k_y} r^{-a} \cos\left(\frac{2\pi}{l_x}(k_x x + \phi_x)\right) \cos\left(\frac{2\pi}{l_y}(k_y y + \phi_y)\right), \tag{50}$$

where $r = \sqrt{k_x^2 + k_y^2}$, $a = 1.5$, and $\phi_{x,y}$ are k_{max}^2 random numbers chosen from the uniform distribution $U(0, 1)$. The integers k_x and k_y range from 0 to $k_{\max} - 1$, where $k_{\max} = 5$.

The amplitude of the perturbation is then scaled such that the maximum initial amplitude $y_a(x)$ above $y = 0$ is $A_0 = 0.1$ ($= 0.88\,\mathrm{pc}$). To keep the interface shape constant across test runs, I always use the same seed for random number generation.

The initial density profile is set to $\rho = \rho_c$ above the interface (for the cloud gas) and $\rho = \rho_h$ below the interface (the halo gas). In two dimensions, the density is given by:

$$\rho(x, y) = \rho_h + \frac{1}{2}(\rho_c - \rho_h)\left[1 + \tanh\left(\frac{y - y_a(x)}{l_y/N_y}\right)\right], \tag{51}$$

where $y_a(x)$ is the initial amplitude of the perturbation given by Equation 48 or Equation 49, l_y is the length of the domain along the y-axis, and N_y is the number of grid cells along the y-axis.

The halo and cloud gas are also in ram pressure equilibrium. The initial conditions for velocity establish this equilibrium and set up the inflow of diffuse halo gas, which creates the ram pressure that drives the instability. The velocity in the x-direction is initially set to be zero (three dimensions: x- and y-directions).

The vertical velocity v_y around the interface is given by the velocity eigenfunction corresponding to the interface perturbations (Eq. 48 and 49):

$$v_y(x, y) = v_h + \frac{1}{2}(v_c - v_h)\left[1 + \tanh\left(\frac{y - y_a(x)}{4l_y/Ny}\right)\right] + A_0 \exp\left(-k|x|\right)\exp\left(-k|y| - y_a(x)\right), \tag{52}$$

where v_h is the velocity of the halo gas, v_c is the velocity of the cloud gas, and k is the wavenumber for sinusoidal waves with spanning the simulation domain in the x-direction:

$$k = \frac{2\pi}{l_x}. \tag{53}$$

The last term in Equation 52 represents perturbation of the velocity, which drives the instability.

In three dimensions, the density profile is similar:

$$\rho(x, y, z) = \rho_h + \frac{1}{2}(\rho_c - \rho_h)\left[1 + \tanh\left(\frac{z - z_a(x, y)}{l_z/N_z}\right)\right], \tag{54}$$

where the the initial amplitude $z_a(x, y)$ comes from Equation 50, l_z is the length of the simulation domain along the z-axis, and N_z is the number of grid cells in the z-direction. The vertical velocity v_z is the velocity eigenfunction corresponding to the three-dimensional interface perturbation (Eq. 50):

$$\begin{aligned} v_z(x, y, z) = v_h + \frac{1}{2}(v_c - v_h)&\left[1 + \tanh\left(\frac{z - z_a(x, y)}{4l_z/Nz}\right)\right] \\ &+ A_0 \exp\left(-k|x|\right)\exp\left(-k|y|\right)\exp\left(-k|z| - z_a(x, y)\right), \end{aligned} \tag{55}$$

To prevent an initial "kick" to the interface, the halo and cloud gas are set up in ram pressure equilibrium:

$$\rho_h v_h^2 = \rho_c v_c^2, \tag{56}$$

i.e., in the rest frame of the interface. The interface is already in thermal pressure equilibrium. Together with the condition on the shock strength for a Mach 2 shock,

$$v_h - v_c = 2c_{s,h}, \tag{57}$$

the ram pressure equilibrium condition results in the diffuse and dense gas inflow velocities

$$v_h = \frac{2c_{s,h}}{1 + \sqrt{\rho_h/\rho_c}} \tag{58}$$

$$v_c = \left(\frac{\rho_h}{\rho_c}\right)^{1/2} \frac{2c_{s,h}}{1 + \sqrt{\rho_h/\rho_c}}, \tag{59}$$

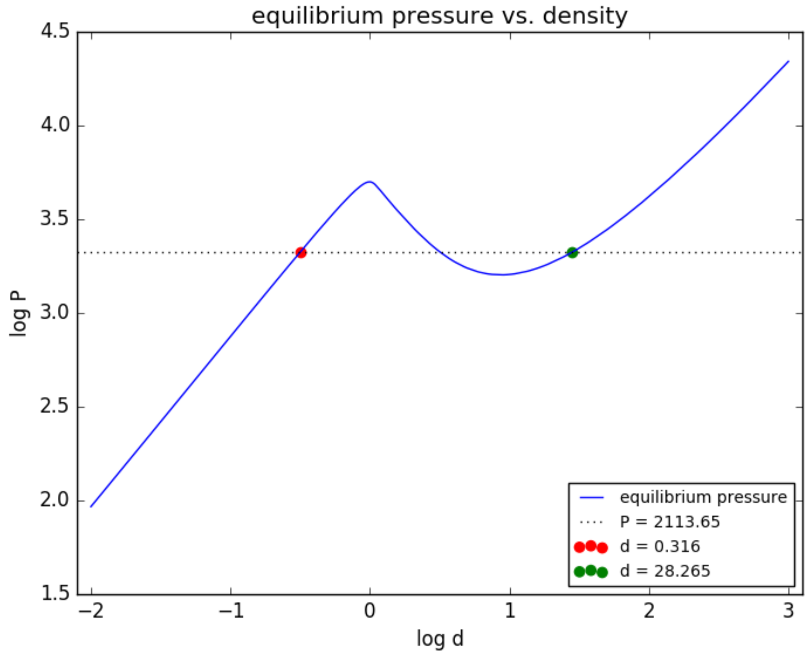

Figure 2: Plot of log P vs. log n for thermal equilibrium. The red and green dots denote the two densities I use for the halo and cloud gas, and the dotted line marks the uniform initial pressure. At these densities and this pressure, the two phases are in thermal equilibrium.

with the sound speed in the hot, diffuse gas

$$c_{s,h} = \sqrt{\frac{P}{\rho_h}}. \tag{60}$$

I determine the initial densities and pressure from Figure 2, which shows pressure as a function of density at thermal equilibrium, as given by the heating and cooling model functions (Sec. 1.2). Based on this plot, I select initial densities that can coexist at the same equilibrium pressure. I select a halo density $\rho_h = 0.316$ and a cloud density $\rho_c = 28.265$, with a uniform pressure $P = 2113.65$ throughout the simulation domain, as required for thermal equilibrium.

2.2.2 Boundary Conditions

I use periodic boundary conditions at the x-boundaries (three dimensions: x- and y-) of the simulation domain. Inflow of hot, diffuse gas occurs at the lower y-boundary (three dimensions: z-), with an upwards inflow velocity of v_h, as given in Sec. 2.2.1. The upper boundary allows for inflow of cold, dense gas, with a downwards velocity of v_c.

The boundary cells are subject to the same corrections of velocity and other quantities, as required for the comoving reference frame (Sec. 2.1.3).

2.2.3 Scalar Fields

Each simulation contains three passive scalar fields, which I use as tracers. At any given point in the domain, the value of a scalar field S can be calculated from the density ρ and the color c of the field:

$$S = \rho c. \tag{61}$$

S_0 marks the interface between the cloud and the halo. It is initialized as a Gaussian distribution around the interface, with a standard deviation of 0.05 ($= 0.44\,\mathrm{pc}$) and a peak color value $c_0 = 1$ at the calculated interface position.

S_1 is used to trace the cloud gas. It is initialized with $c_1 = 1$ in the dense cloud gas and $c_1 = 0$ in the diffuse halo gas.

S_2 traces the inflow of gas that enters the simulation domain at the lower boundary in y (three dimensions: z) and flows upward toward the halo-cloud interface. All gas initially within the simulation domain, as well as gas in the ghost cells at the upper boundary, receives a color $c_2 = 0$. Only gas flowing in from the lower boundary is given $c_2 = 1$.

2.2.4 Magnetic Fields

For the RTI driven by ram pressure, the critical field strength (Eq. 37) can be written as

$$\begin{aligned} B_c &= \left(L \frac{\rho v^2}{\Sigma} (\rho_2 - \rho_1) \right)^{1/2} \\ &= \left(L \frac{\mathcal{M}^2 P_1}{\Sigma} (\rho_2 - \rho_1) \right)^{1/2}, \end{aligned} \tag{62}$$

where P_1 is the thermal pressure in the diffuse gas and $\mathcal{M}$ is the Mach number of the inflow. Alternatively, B_c can be expressed as the critical ratio between thermal and magnetic pressure, or the plasma β,

$$\begin{aligned} \beta_c &= \frac{8\pi P_{\mathrm{therm}}}{B_c^2} \\ &= 25 \frac{\kappa}{\mathcal{M}^2} \end{aligned} \tag{63}$$

for the specific simulation parameters used. Here, κ is the number of wave modes in the interface.

For the 2D models, I explore a sequence of plasma β, from $\beta_c/2$ to $32\beta_c$, to highlight the difference between the ram pressure- and gravity-driven magnetized RTI. The domain is initialized with a constant magnetic field in the x-direction.

2.3 Heating and Cooling

I use Athena's third-order Runge-Kutta (RK3) method to integrate Equations 38-41. Within the RK3 integrator, safeguards are established to prevent non-physical results: if the internal energy or the density becomes negative, the RK3 algorithm will retry the integration up to five times, halving the timestep for each attempt.

Heating and cooling are implemented as a source term in the total energy equation (Eq. 40) through subcycling: the radiative losses are applied via an embedded Runge-Kutta-Fehlberg (RK45) algorithm within the RK3 substeps. The RK45 integrator uses an adaptive step size and contains safeguards to guarantee a positive temperature and limit the temperature change of each RK45 step. Subcycling is necessary since the cooling timescale is usually at least one order of magnitude shorter than the timestep imposed by the Courant-Friedrichs-Lewy stability condition.

2.4 Definitions

Here, I briefly discuss two measures used to quantify and analyze the simulation results: the interface amplitude as a measure for the instability growth (Sec. 2.4.1), and the mixing length as a measure for mixing between the cloud and halo gas (Sec. 2.4.2).

2.4.1 Amplitude

The amplitude of the instability is defined as the root-mean-square (RMS) deviation of the y-position (three dimensions: z-position), weighted by the passive scalar field S_0, which marks the interface.

The amplitude A is given by

$$A = \left(\frac{\sum_{i,j} \left(y[i,j] - \langle y \rangle\right)^2 \cdot S_0[i,j]}{\sum_{i,j} S_0[i,j]} \right)^{1/2}, \tag{64}$$

where the scalar-weighted mean y-position $\langle y \rangle$ is

$$\langle y \rangle = \frac{\sum_{i,j} y[i,j] \cdot S_0[i,j]}{\sum_{i,j} S_0[i,j]}. \tag{65}$$

2.4.2 Mixing Length

The measurement of mixing length is based on the work of Cook et al. (2004) and Cabot & Cook (2006), as summarized by Zhou (2017). I modify their approach to use the color of the passive scalar field S_1, initialized with color $c_1 = 1$ in the cloud gas and $c_1 = 0$ in the halo gas, accounting for the case of non-reacting and incompressible gases in my simulations. The mole fraction X of the dense (cloud) gas at any point within the simulation domain is given by

$$X = \frac{c - c_h}{c_c + c_h}, \tag{66}$$

where c_c and c_h are the respective colors of the cloud and halo gas, and c is the color of the scalar field S_1 at that point. The mole fraction X_P of perfectly mixed gas (consisting of halo and cloud gas in equal parts) is

$$\begin{aligned} X_P(X) &= \begin{cases} 2X & \text{if} X \leq 1/2 \\ 2(1-X) & \text{if} X > 1/2 \end{cases} \\ &= 2 \min(X, 1-X). \end{aligned} \tag{67}$$

The mixing length h is then calculated as follows:

$$h = \int_{y_1}^{y_2} X_P(\langle X \rangle) \, dy, \tag{68}$$

where y_1 and y_2 are the lower and upper boundaries of the simulation domain in the two-dimensional case. (In three dimensions, h is determined by taking this integral from z_1 to z_2 with respect to z.)

If the halo and cloud gas were perfectly mixed in x (three dimensions: in x and y), this mixing length would be the height of the corresponding layer of mixed gas (Cook et al. 2004; Cabot & Cook 2006).

3 Results

I will start by assessing the impact of numerical resolution on the simulation results (Sec. 3.1), using the two-dimensional simulations. The three-dimensional RTI is explored in Sec. 3.2, and I discuss the effects of magnetic fields in Sec. 3.3.

3.1 Resolution Study in Two Dimensions

To assess the impact of resolution, I perform a resolution study in two dimensions, first testing the adiabatic case, then adding heating and cooling. The simulation domain is of size $L \times 2L$, with $L = 1.0 = 8.8\,\mathrm{pc}$. For a given resolution N, the computational grid is of size $N \times 2N$ cells, and so each side of a grid cell measures L/N in length. I test resolutions $N = 128$, 256, 512, and 1024, denoted as N128, N256, N512, and N1024, respectively. All times are given in code units.

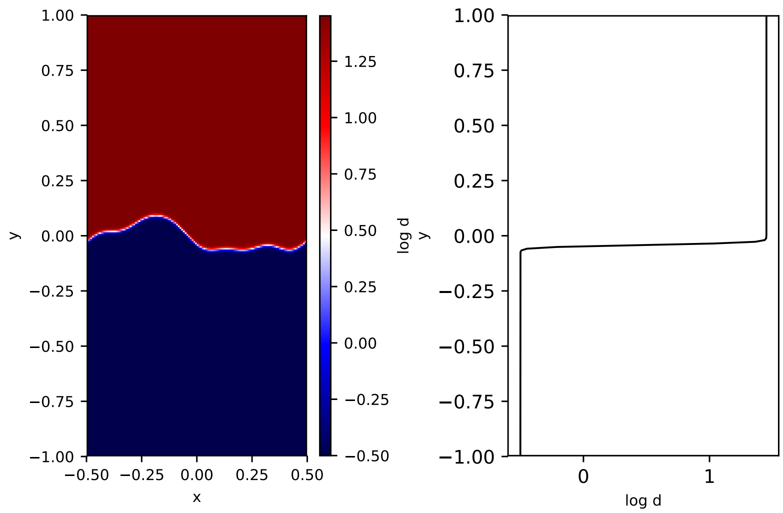

Figure 3: Logarithm of the gas density at $t = 0$ for the two-dimensional RTI. Map is shown on the left, and a profile taken along the y-direction at $x = 0$ is shown on the right.

3.1.1 Adiabatic Models

Figure 3 shows the initial density profile for the two-dimensional RTI. This same perturbation shape and strength is used for the initialization of each run.

Figure 4 contains snapshots of the density (d) for each of the four test resolutions: N128, N256, N512, and N1024. In the adiabatic case, the initial shock from the halo gas quickly affects the cloud gas. The transition region between the fluids expands toward the upper boundary. At $t = 0.05$, the interface remains within the grid, but by $t = 0.1$ it has reached the y-boundaries, leaving only halo gas and the mixing region behind. By $t = 0.4$, the grid is filled with turbulent mixing of the halo and cloud gas. Since the perturbations are now limited by the imposed boundary values, the results cannot be used for physical interpretation at this time. The effect of the boundaries can be seen for N128 in Fig. 4 (bottom left) as a thin blue region at the bottom.

Additionally, careful inspection of the plots in Figure 4 reveals the effects of resolution. Higher resolutions provide finer detail and show evolution on smaller scales. Moreover, although they are generally similar, the density profiles appear slightly different at each resolution. To evaluate the impact of these small discrepancies, I compare the amplitude A (Eq. 64) and the mixing length h (Eq. 68) of the instability in each run. Figure 5a shows the amplitude plotted against time, and Figure 5b shows the mixing length. The linear growth phase until $t = 0.05$ is nearly independent of resolution, yet, once secondary instabilities and eventually turbulence develop, the models start to differ. Figure 5a shows that N128 diverges slightly from the others, but N256, N512, and N1024 are in close agreement until $t \sim 0.1$, by which point the interface has reached the upper and lower boundaries. Similarly, the time evolution of the mixing lengths is roughly the same at each resolution until $t \sim 0.1$.

3.1.2 Radiative Models

For runs including radiative losses (heating and cooling), the interface perturbation has the same shape as in the adiabatic case, as shown in Figure 3.

Figure 6, like Figure 4, shows snapshots of the density at $t = 0.05$, 0.1, and 0.4. While the interface reaches the boundaries by $t = 0.1$ in the adiabatic case, the radiative losses keep the transition region between the halo and cloud gas more compressed. Rapid cooling leads to a pressure drop, and thus to a density increase, until the thermal pressure in the cold dense gas approximately equals the ram pressure (e.g., Vázquez-Semadeni et al. 2006). Thus, given the same mass inflow, the interface can "accrete" more mass than in the adiabatic case within the same volume. Therefore, the interface remains contained within

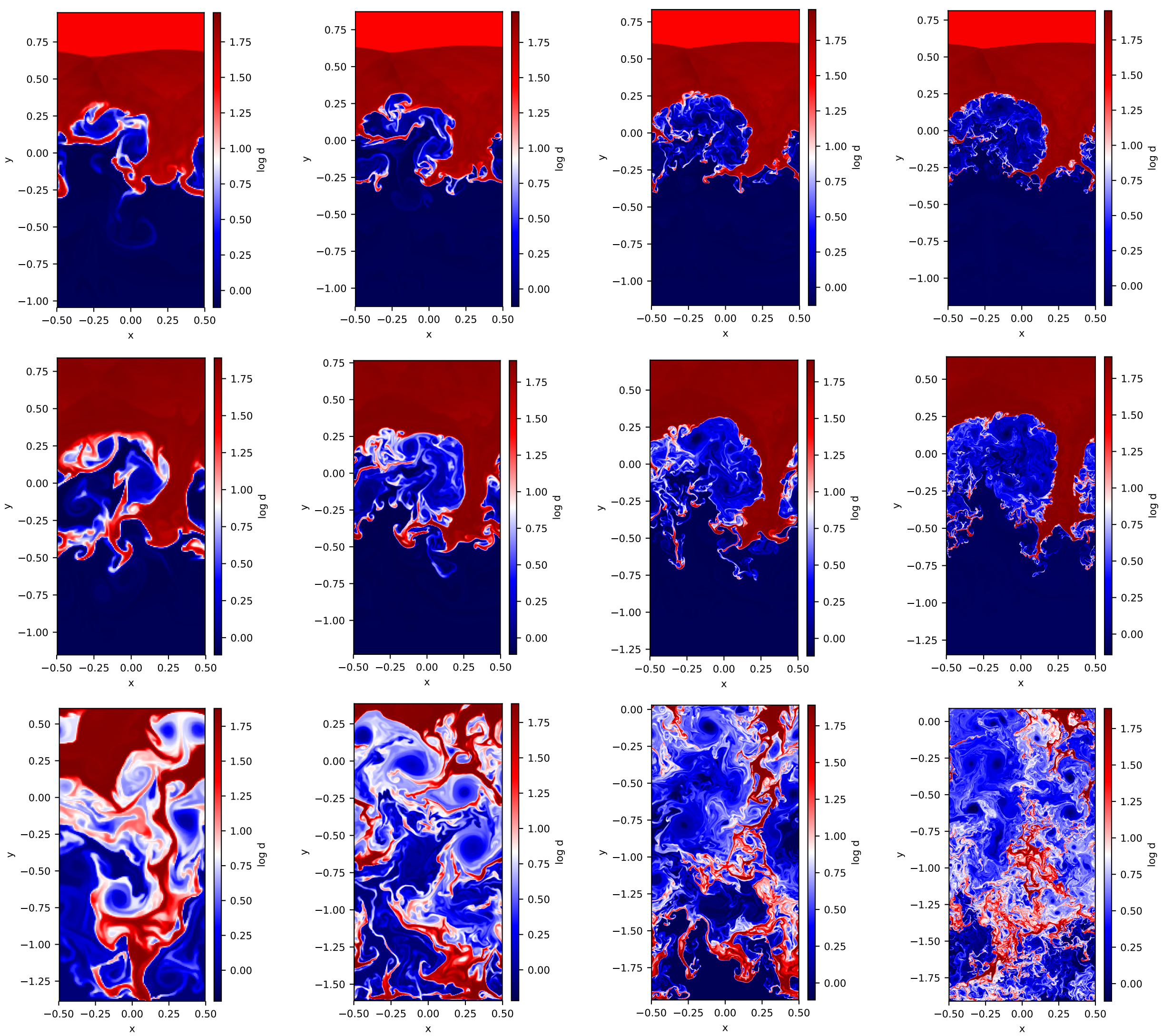

Figure 4: Evolution of the adiabatic instability in 2D at $t = 0.05$, 0.1, and 0.4 (top to bottom). Resolutions are N128, N256, N512, and N1024 (left to right). While the overall shape stays the same with increasing resolution, small-scale structure increasingly develops.

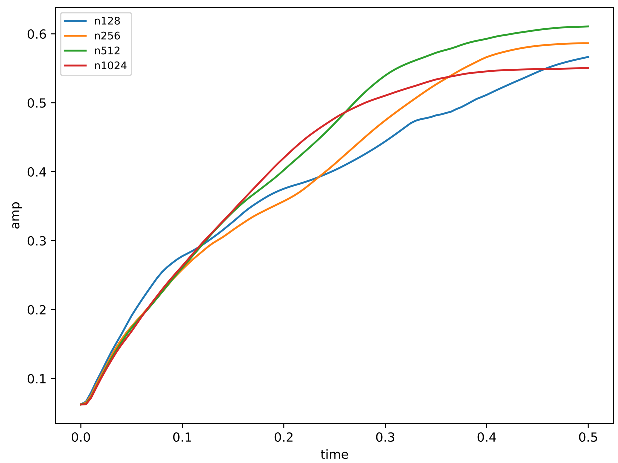

(a) Amplitude vs. time.

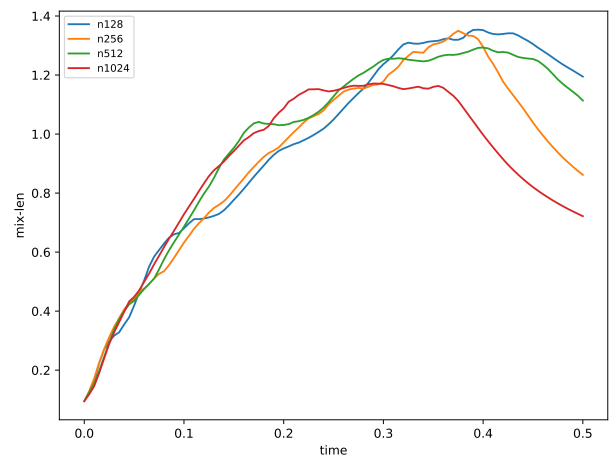

(b) Mixing length vs. time.

Figure 5: Amplitude and mixing length vs. time for the adiabatic instability in 2D (N128, N256, N512, and N1024). The linear growth phase until $t \sim 0.05$ is nearly independent of resolution. The results slightly diverge once turbulence develops.

the simulation domain, allowing for a longer time span to follow the evolution of the instability.

The effects of resolution can be observed in Figure 6 as well. As in the adiabatic case, higher resolution yields finer detail and shows the small-scale evolution of the instability. Additionally, the density profiles at each resolution show small differences despite their general similarity in shape and size.

Figure 7 shows the amplitude and mixing length plotted against time for each of the four test resolutions. The amplitudes (Fig. 7a) are similar until $t \sim 0.1$, at which point the runs diverge. For the mixing lengths (Fig. 7b), the similarity lasts until $t \sim 0.15$. The mixing lengths then begin to decrease, suggesting that the instability reaches saturation around that time. Amplitude and mixing length generally appear to increase with higher resolution; however, N512 shows fluctuations not observed at other resolutions—a noticeable decrease in amplitude while that quantity increased in other runs, as well as a sharper decline in mixing length.

3.2 The Three-Dimensional RTI

In three dimensions, the simulation domain is of size $L \times L \times 2L$, with $L = 1.0 = 8.8\,\mathrm{pc}$, corresponding with a computational grid of size $N \times N \times 2N$ cells for a given resolution N. I explore both the adiabatic and radiative versions of the instability at resolutions N128 and N256.

The initial density profile for the three-dimensional RTI is shown in Figure 8. This perturbation shape and strength is used for all 3D runs.

Figure 9 shows the evolution of the instability for the adiabatic and radiative cases. Snapshots of the mean density along the x-direction are shown for $t = 0.05$, 0.1, and 0.4. As in the two-dimensional runs, the interface quickly reaches the lower and upper boundaries in the adiabatic version. When heating and cooling are included, the interface remains within the grid, providing a more meaningful look at the instability and its evolution. The two resolutions N128 and N256 produce generally similar results.

Figure 10 shows the amplitude and mixing length plotted against time for N128 and N256 (both the adiabatic and radiative models). The adiabatic amplitude and mixing length measurements lose meaning by the time the interface has expanded past the upper z-boundary (between $t = 0.05$ and $t = 0.1$ in the adiabatic case); however, the results for N128 and N256 are the same until this point of divergence. For the radiative case, N128 and N256 are in near-perfect agreement up through $t = 0.4$, at which point the interface and mixing region still remain within the grid (Fig. 9). The inclusion of cooling keeps the mixing region more compressed and slows the instability growth.

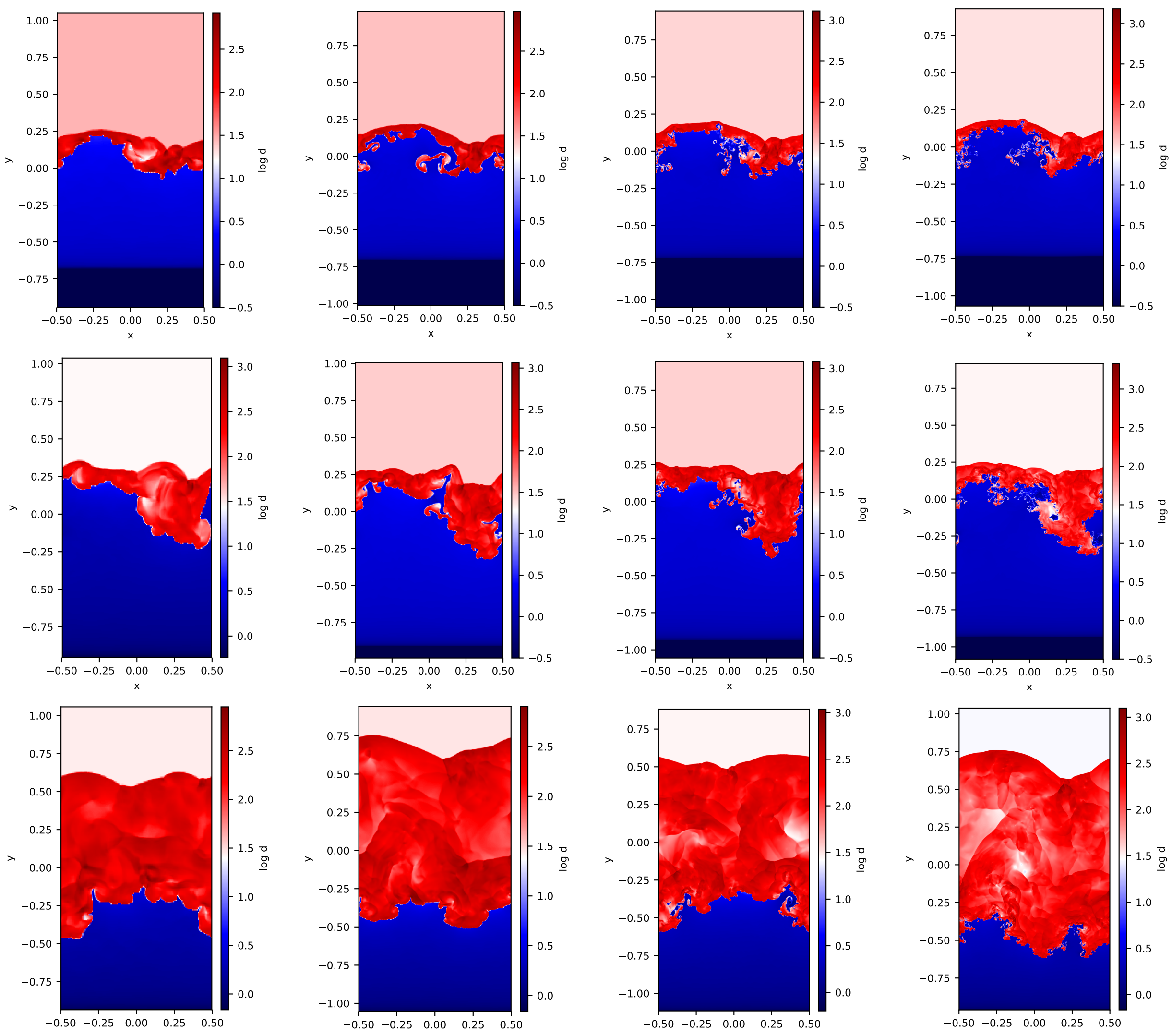

Figure 6: Evolution of the instability in 2D with radiative losses at t = 0.05, 0.1, and 0.4 (top to bottom). Resolutions are N128, N256, N512, and N1024 (left to right). Due to the rapid cooling, the interface now stays contained within the simulation domain.

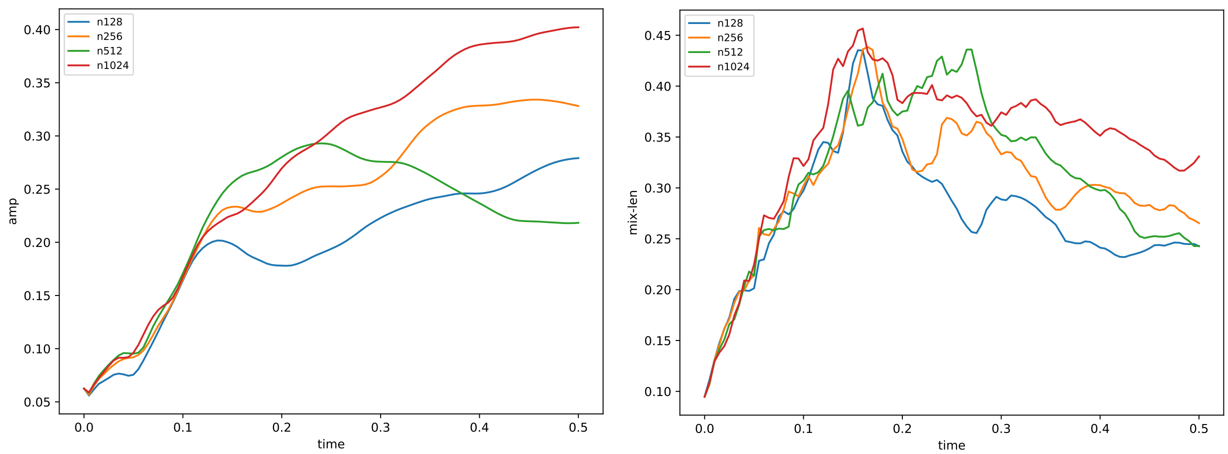

(a) Amplitude vs. time.

(b) Mixing length vs. time.

Figure 7: Amplitude and mixing length vs. time for the instability in 2D with radiative losses (N128, N256, N512, and N1024). Growth is relatively independent of resolution until $t \sim 0.1$ for amplitude and $t \sim 0.15$ for mixing length.

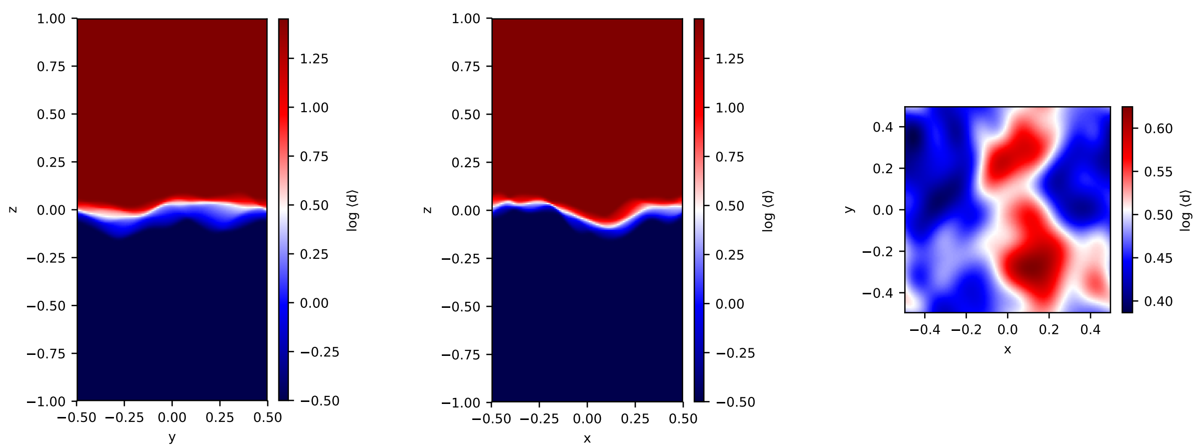

Figure 8: Initial density profile for the three-dimensional RTI. Left to right: views along the x-, y-, and z-directions. Shown is the mean density along each direction. This initial profile is used for every 3D run.

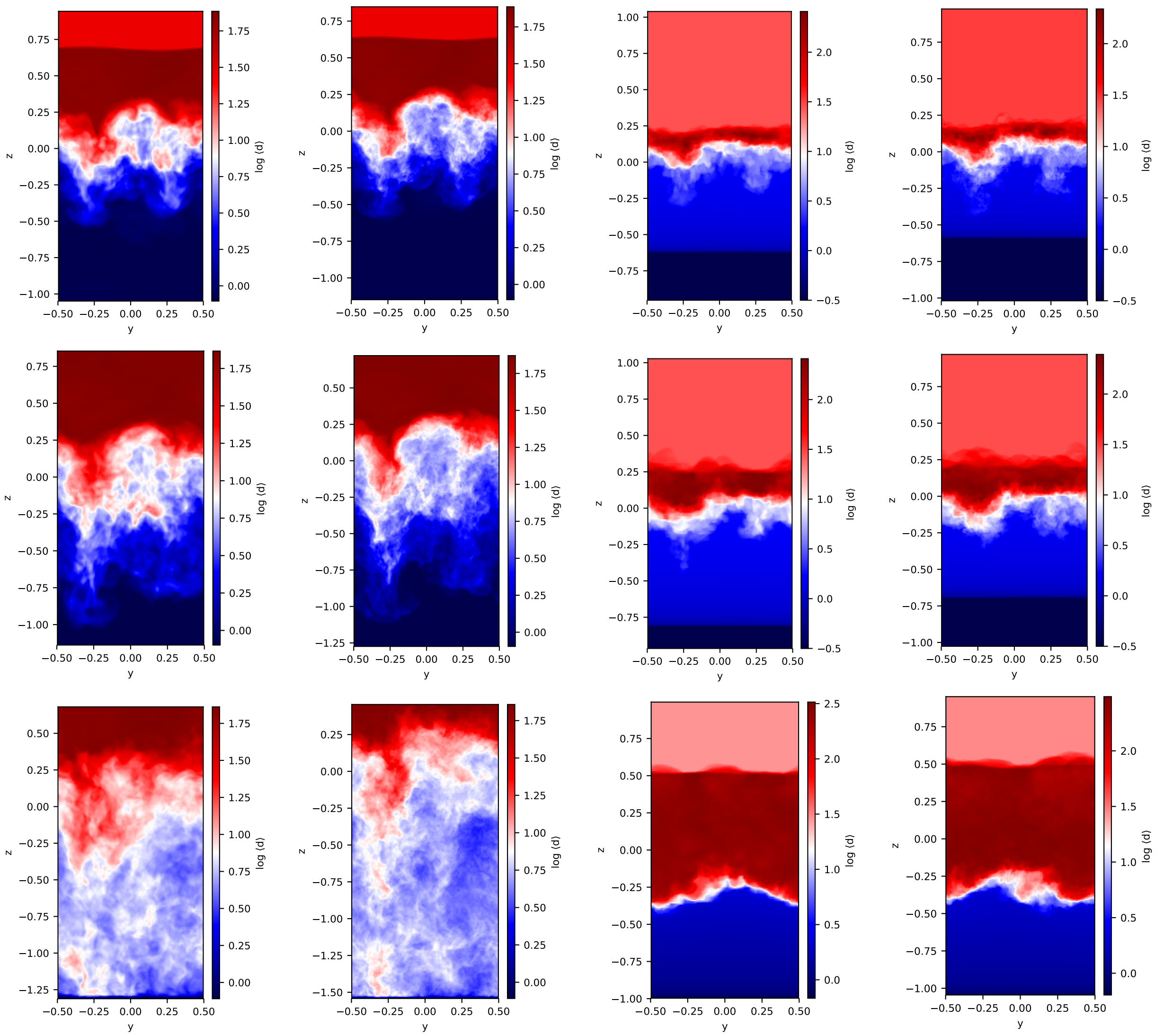

Figure 9: Evolution of the instability in 3D at $t = 0.05$, 0.1, and 0.4 (top to bottom). Resolutions are N128 (first and third columns) and N256 (second and fourth columns). The first two columns show the adiabatic instability; the second two show the runs with cooling. All plots show the mean density along the x-direction. Small-scale structural differences due to resolution can be seen. The interface is contained within the simulation domain in runs with cooling.

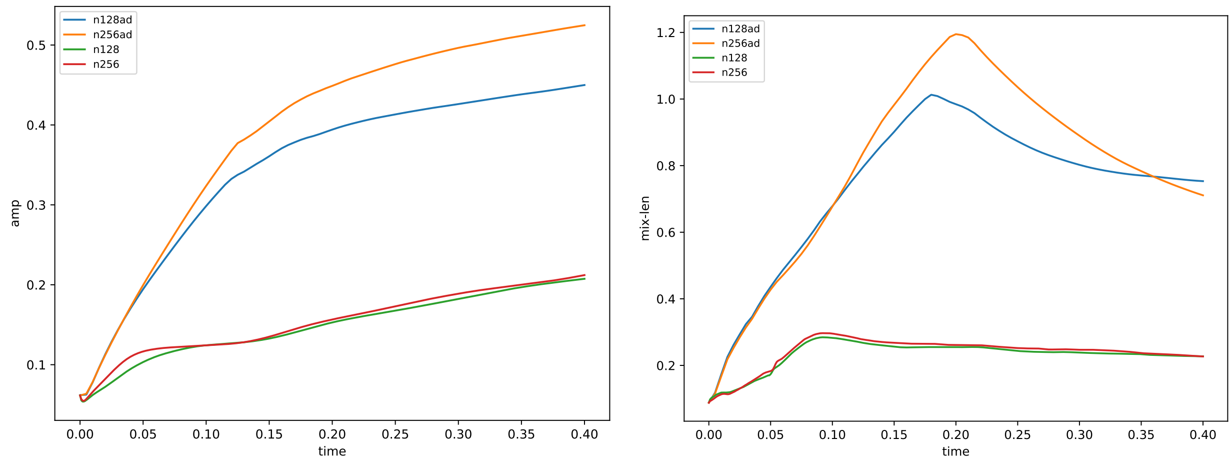

(a) Amplitude vs. time.

(b) Mixing length vs. time.

Figure 10: Amplitude and mixing length vs. time for the instability in 3D. Both adiabatic ("ad") and radiative runs are shown. Cooling keeps the interface more compressed, slowing the instability growth.

3.3 Magnetic Fields

I assess the effects of magnetic fields on the RTI in two and three dimensions. I also test both adiabatic and radiative models to evaluate the combined impact of cooling and magnetic fields.

3.3.1 Magnetic Fields in Two Dimensions

Magnetic fields aligned with the interface can suppress the RTI in two dimensions by providing an effective surface tension (Sec. 2.2.4). Since the gravitational acceleration is replaced by an acceleration term proportional to the ram pressure, the resulting critical field strength will scale with the Mach number of the inflow, $\mathcal{M}$ (Eq. 37).

Yet Figure 11a suggests that the estimate for the critical field strength is not correct. Starting at half the critical plasma β_c and running up all the way to $32\beta_c$, the instability progressively develops, but never reaches the hydrodynamical ($B = 0$) amplitude. Figure 12 provides a more detailed view. The top row shows snapshots of the density field at $t = 0.05$ for the adiabatic runs, with the plasma β increasing from left to right (i.e., the magnetic field gets weaker from left to right). At the highest field strength (lowest β), the interface develops a sinusoidal shape facing the low-density gas. The magnetic tension component of the Lorentz force counterbalances the ram pressure imbalance, and the perturbation amplitudes eventually decrease with time (see also Fig. 11a). With decreasing field strength, two effects occur. The perturbations become more pronounced, consistent with the critical field strength argument, and perturbations at higher wavenumbers start to grow, which is expected from the scale-dependency of the critical field strength (Eq. 37).

The situation is more extreme for the cooling runs (Fig. 11b and bottom row of Fig. 12). Even a small magnetic field suppresses instability growth, yet the same tendency as for the adiabatic sequence can be observed: with decreasing field strength, the amplitudes tend to grow. The main difference from the adiabatic models is the radiative losses, increasing the density in the cloud gas. The density (and thus the magnetic field) increase can be roughly estimated by balancing the pressures, assuming that the cloud gas is initially at rest, and that the magnetic pressure is negligible compared to the thermal and ram pressure:

$$\rho_c = \frac{1}{c_c^2}\left(P + \rho_h v_h^2\right), \tag{69}$$

which for the model parameters results in $n_c = \rho_c/m_H = 140$, or 5 times the original cloud density.

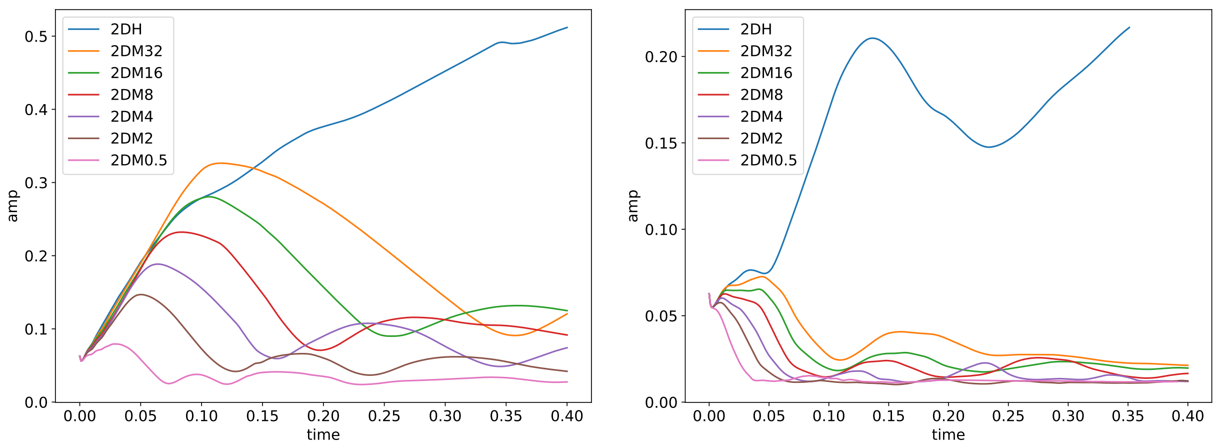

(a) Adiabatic MHD models. (b) MHD models with cooling.

Figure 11: Amplitude of the interface layer (Eq. 64) against time. For the adiabatic case, the instability should grow for $\beta > \beta_c$, but it only fully develops for $\beta > 16\beta_c$. No instability growth is observed for the cooling case.

3.3.2 Magnetic Fields in Three Dimensions

As shown by Chandrasekhar (Sec. 1.3), a magnetic field parallel to the interface between the halo and cloud gas should have no impact on modes perpendicular to $\vec{B}$, while modes parallel to $\vec{B}$ are suppressed for fields $B > B_c$, where B_c is the critical field strength given by Eq. 62. Therefore, while growth along the x-direction was suppressed in 2D runs, for 3D runs some growth along the y-direction can be expected.

Figure 13 compares the evolution of the instability (including radiative losses) with and without a magnetic field in two and three dimensions. The magnetic field does suppress the growth of the instability in two dimensions (as shown also in Sec. 3.3.1). In three dimensions, however, the instability grows in the presence of magnetic fields. Applying a magnetic field results in a more clearly defined interface, as well as the growth of large "fingers" downwards. The top of the interface remains relatively flat and reaches the upper boundary of the grid by $t = 0.2$.

Figure 14 contains snapshots of the density at $t = 0.0$, 0.05, and 0.1. The views along the z-axis show that variations in the x-direction are smoothed away as time passes, leaving perturbations along the y-direction. This development matches the theoretical expectations for the magnetic field in the x-direction.

4 Discussion

Not only magnetic fields, but also radiative losses, can strongly affect the evolution of the RTI. While magnetic fields give rise to an effective surface tension and thus introduce anisotropy in three dimensions, leading eventually to super-hydrodynamical growth rates, radiative losses result in rapid mass accumulation and eventually fragmentation of the initial (large-scale) instability modes. Combining magnetic fields and radiative losses in three dimensions recovers the instability.

4.1 Heating and Cooling Effects

Models that include heating and cooling show relative containment of the interface between the cloud and halo gas. In adiabatic runs, the interface quickly reaches the lower and upper boundaries. However, runs with cooling show a smaller mixing region between the cloud and the halo gas, which can be attributed to the radiative losses. As Vietri et al. (1997) have shown in the context of the Kelvin-Helmholtz instability, radiative losses should result in relative confinement of the mixing region and turbulence around the interface. This physical effect does appear in my simulations of the RTI, where the interface and the mixing region remain more compact and stay within the grid for far longer than in the adiabatic case. The three-dimensional

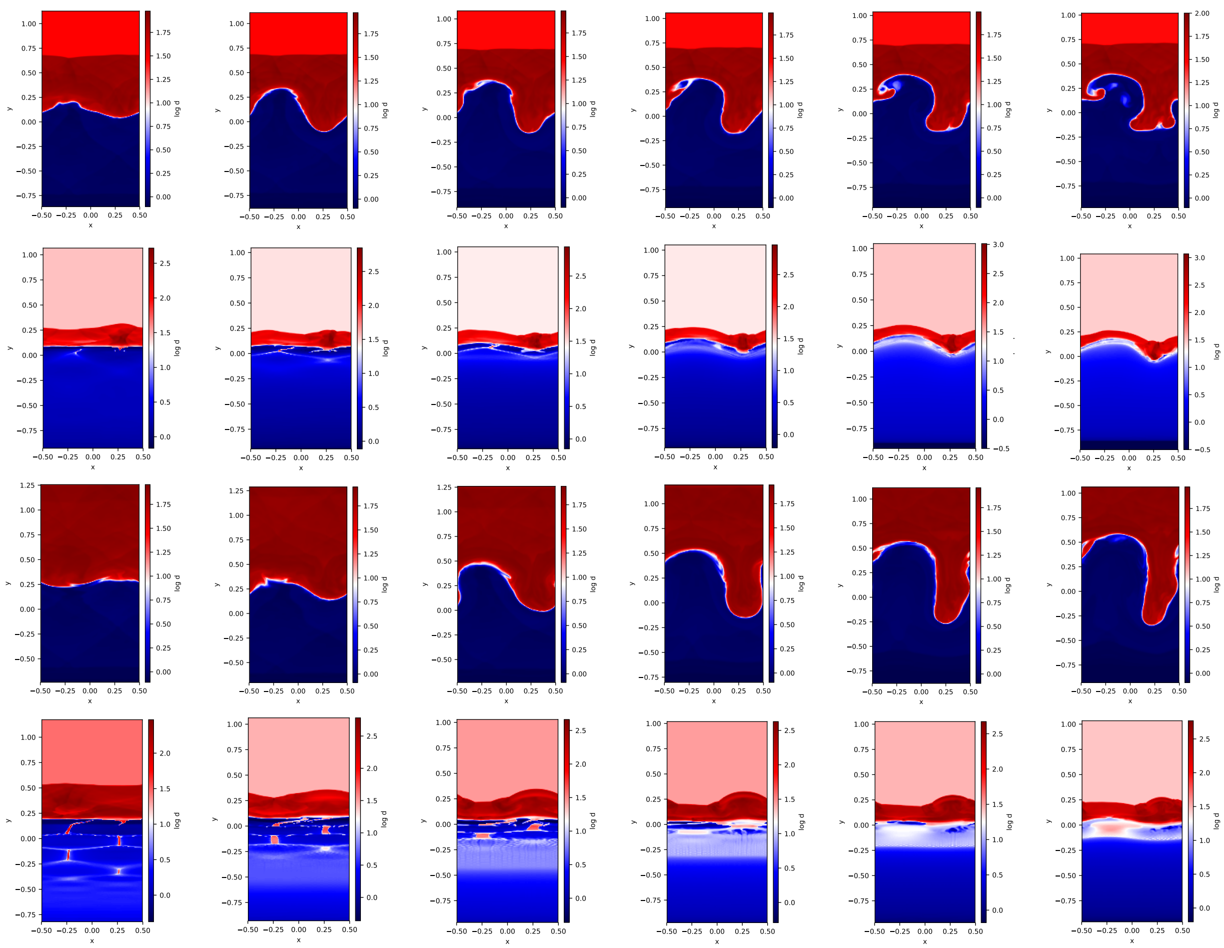

Figure 12: Density snapshots of the adiabatic MHD runs (1st and 3rd row) and the cooling runs (2nd and 4th row), taken at $t = 0.05$ (top two rows) and $t = 0.1$ (bottom two rows). Instability growth is strongly suppressed in the cooling runs, while the adiabatic runs develop instability with decreasing field strength. Models are shown for $\beta = 1/2$, 2, 4, 8, 16, $32\beta_c$ (left to right).

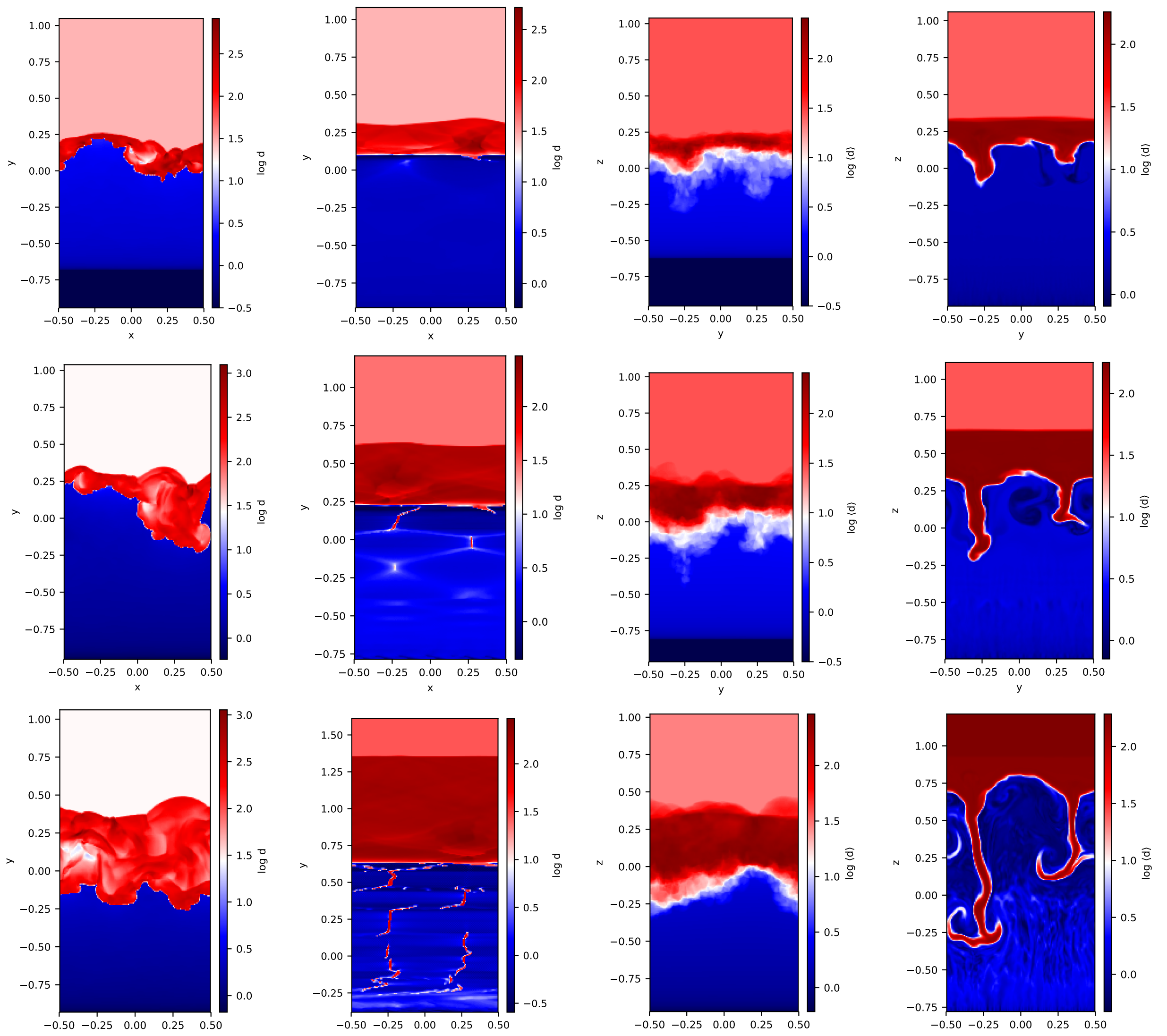

Figure 13: Comparison of the 2D and 3D hydro and magnetic models. Shown are snapshots at $t = 0.05$, 0.1, and 0.2 (top to bottom) for N128. First pair of columns is 2D and second pair of columns is 3D (viewed along the x-direction). The 2nd and 4th columns include a magnetic field with $\beta = 8$. The 3D magnetic field run develops instability more strongly than its hydrodynamical counterpart.

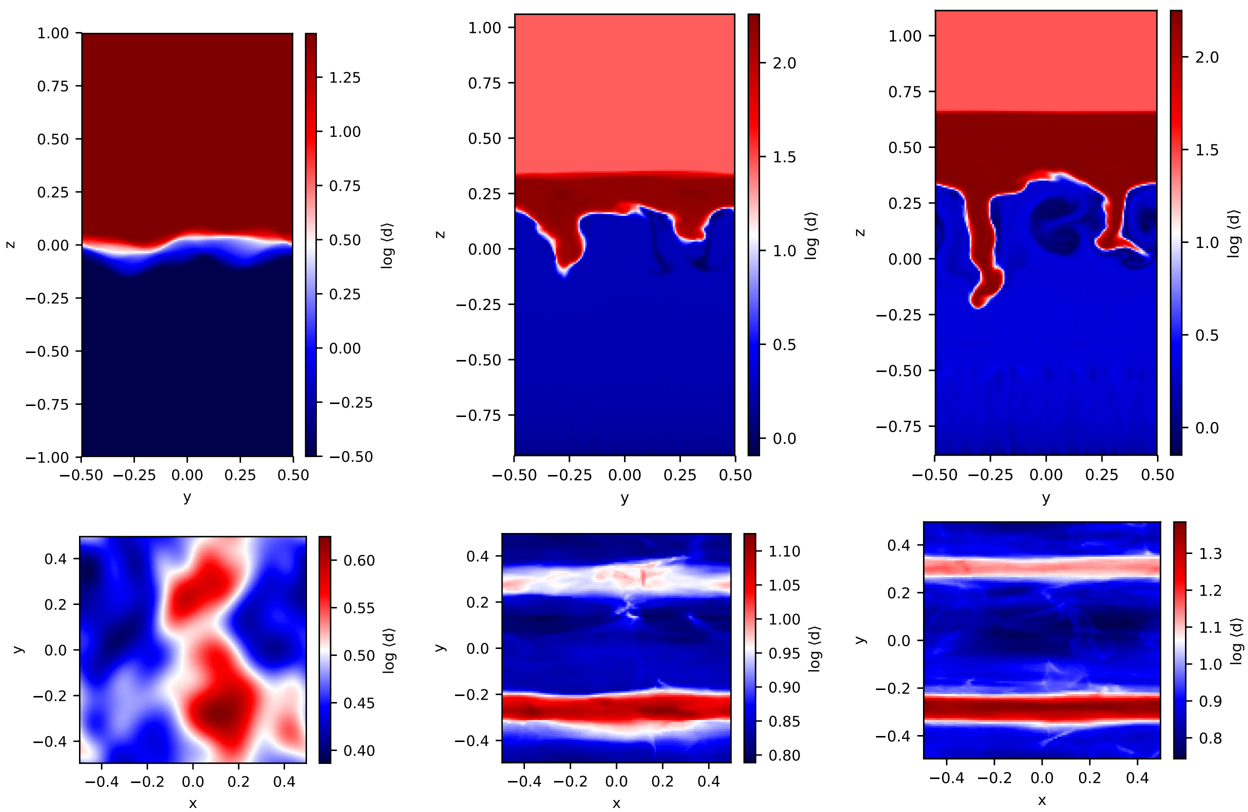

Figure 14: Density snapshots at t = 0.0, 0.05, and 0.1 of the radiative magnetic 3D runs, with resolution N128. Top row: view along x-direction. Bottom row: view along z-direction. This highlights the anisotropy introduced by the magnetic field, eventually leading to instability growth.

simulations (Sec. 3.2) show that the inclusion of radiative cooling results in slower growth of the amplitude and mixing length (Fig. 10).

A closer look at the interface evolution suggests that most of the dense gas accumulating comes from the cloud: i.e., the cloud "self-shields" against disruption. Cooling times in the dense gas are substantially shorter than in the diffuse gas. Therefore, while the diffuse halo gas develops a shock (see top right panel in Fig. 13), the dense cloud gas just accumulates. For a realistic (not plane-parallel) cloud geometry, the shock in the diffuse gas would be the bow shock.

4.2 Magnetic Field Effects

The magnetic instability criterion for the gravity-driven RTI needs to be modified (see Eq. 37) to account for the ram pressure as the source of acceleration. Yet, even with this modification, the simulation results suggest that another effect needs to be taken into account: instability for weak magnetic fields does initially grow, but magnetic tension forces eventually dominate. The reason for the difference in evolution compared to the gravity-driven RTI lies in the compressibility of the fluid. Considering the conservation laws in magnetohydrodynamical shocks (e.g., Shu 1992), the post-shock field scales as the post-shock density, whose contrast is limited for an adiabatic shock by the ratio $(\gamma-1)/(\gamma+1) = 4$ for $\gamma = 5/3$. Therefore, the critical field strength criterion should be modified by the expected magnetic field increase, as long as the fields are aligned with the interface.

Because of the higher density contrasts, the critical field is even smaller for interfaces with radiative losses, dramatically increasing the ability of magnetic fields to suppress the instability.

The assumption of a completely uniform magnetic field in the inflows is probably highly idealized, even under the assumption of magnetic draping around the cloud (Dursi & Pfrommer 2008). Tangled fields around radio bubbles can stabilize the bubbles if the coherence length of the field is larger than the bubble size scale (Ruszkowski et al. 2007). Figure 15 provides a related view point. It shows snapshots of four 3D runs, taken at $t = 0.1$. The hydrodynamical run (left) and the tangled field model are nearly indistinguishable, while the uniform field model shows strong instability growth. The reason for this behavior can be inferred from Figure 16. The amplitude for the uniform field case (3DM1) increases strongly due to compression and leads to an interface growth above the hydrodynamical rate. Both tangled field cases show slower growth. The right-hand plot of the same figure shows the magnetic energy evolution. When the tangled field gets compressed, the field reversals lead to magnetic energy dissipation, thus lowering the effective magnetic energy in the interface available for resisting compression and bending. Thus, the structures overall resemble more the hydrodynamical results.

4.3 Effects of MPI Parallelization on Results

Athena uses a domain decomposition of the simulation domain for parallelization. Each processor owns a block, representing a part of the full domain. During each integration step (or sub-step, in case of the RK3 integrator), the boundary conditions for each sub-domain are initialized using information from the neighboring domains or the physical boundaries, and then the conserved variables are updated. Processors communicate with each other via the Message Passing Interface (MPI). I noticed that changing the processor arrangement for one and the same simulation led to growing differences in the interface amplitude and other quantities. This only occurs when using the comoving grid, and it is a well-documented consequence of the fact that the `MPI_Allreduce` call to calculate the center-of-mass velocity for the interface (Sec. 2.1.3) is subject to floating-point round-off errors. Addition in floating-point arithmetic is not associative at the level of round-off errors, and the MPI standard does not specify in which sequence `MPI_Allreduce` sums over the domains. While the differences are of lesser importance during the linear growth phase, especially in the adiabatic case (Fig. 5), they are substantially more pronounced in the non-linear phase, especially for the models with cooling (Fig. 7). This is not a consequence of different initializations due to changing random number sequences: the random number sequence is always started with the same seed, and the specific way I initialize the perturbations (via the random phases that are independent of the resolution) guarantee that the interface is the same across different resolutions and domain decompositions.

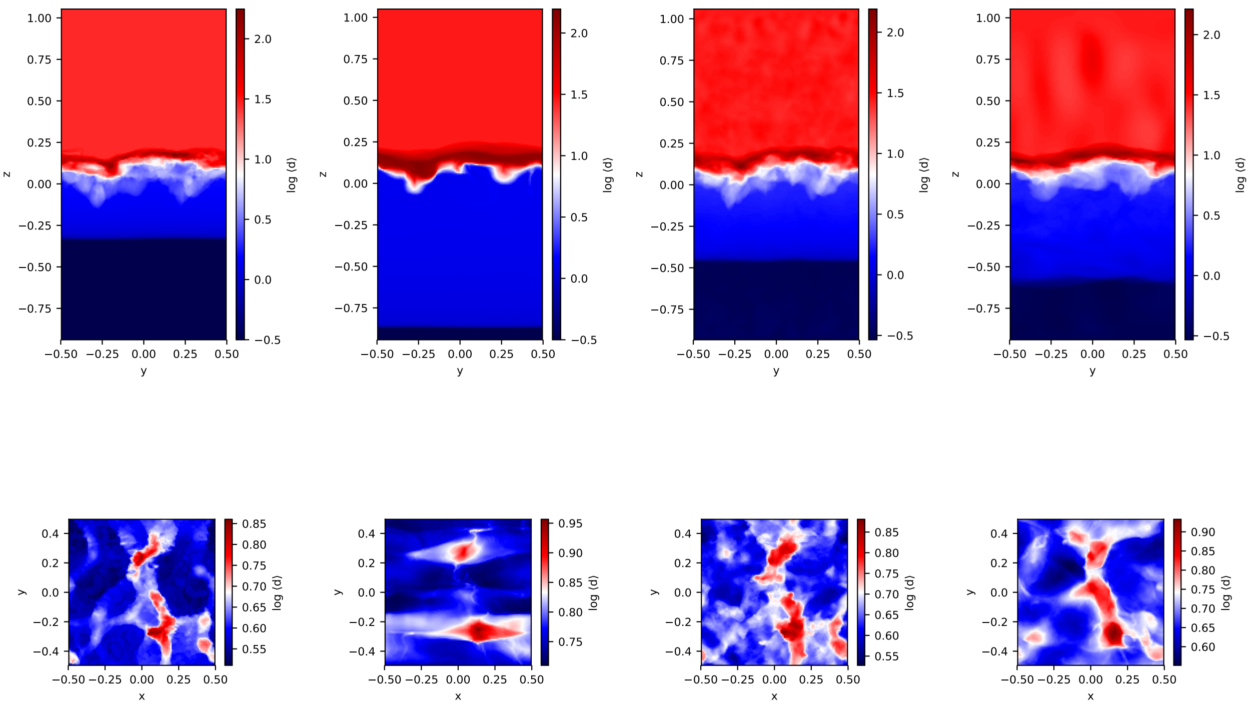

Figure 15: Density snapshots of radiative 3D runs at $t = 0.1$. From left to right: no field, uniform field, tangled field, tangled field limited to large-scale perturbations. Top row: view along x-direction. Bottom row: view along z-direction. Results for the tangled field more closely resemble the hydrodynamical results than in the case of a uniform field.

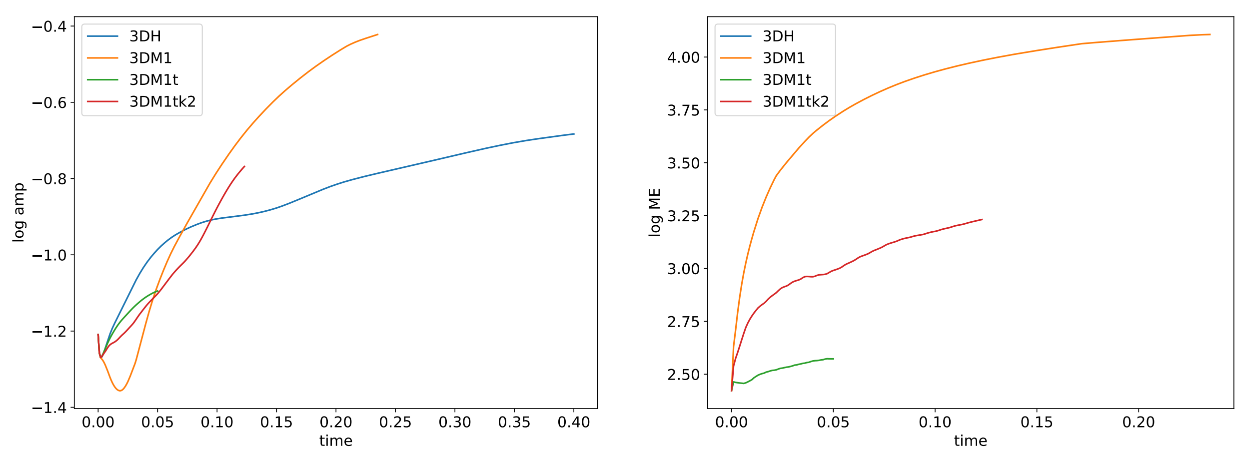

Figure 16: Amplitude and magnetic energy evolution for the four 3D runs: hydro, uniform field, tangled field, and tangled field at large wavelengths. The uniform field run shows faster growth and more magnetic energy than the tangled field runs, which are more like the hydrodynamical case.

5 Conclusions & Outlook

I have presented numerical simulations of the ram pressure-driven Rayleigh-Taylor instability (RTI) in the context of high velocity clouds (HVCs) traveling through the Galactic halo. The RTI is thought to be one of the dominant instabilities leading to the eventual disruption of HVCs. My models address an idealized scenario of RTI evolution at the leading surface of a HVC interacting with the ambient halo gas. Solving the equations of ideal magnetohydrodynamics with the grid-based fluid dynamics code Athena (Stone et al. 2008), I have simulated the instability and its growth at the interface between the hot, diffuse halo gas and the cold, dense cloud. I have performed a systematic investigation of the instability through step-by-step addition of physics relevant to HVCs—radiative losses and magnetic fields.

The results suggest that cooling leads to rapid fragmentation of the halo-cloud interface, thus dampening the instability. This is consistent with the findings of Vietri et al. (1997) and others. In two dimensions, my models reproduce the expected effect of magnetic fields parallel to the interface suppressing the instability. When cooling is included, they do so very efficiently as a result of the higher field strength in the post-shock region. As the field strength decreases, perturbations with higher wavenumbers can grow. In three dimensions, however, the magnetic fields do not suppress the instability, consistent with Stone & Gardiner (2007). Perturbations parallel to the magnetic field are suppressed, but perpendicular perturbations still grow, exceeding the hydrodynamical growth rates given by Chandrasekhar (1961). Tangled magnetic fields produce results more similar to the hydrodynamical case due to turbulent dissipation of the magnetic energy, yet the instability grows more slowly than for a uniform field, possibly because some of the driving energy is lost due to field dissipation. In the context of HVCs, magnetic draping or tangled magnetic fields may be more realistic models for the magnetic field. Further evaluation of these field configurations could provide better insight into the ram pressure-driven RTI and its role in the disruption of HVCs. Finally, the plane-parallel geometry assumed in my models does not take into account mass flow around (and away) from the interface. In that sense, the instability growth found in my models is likely an upper limit compared to more realistic situations.

References

Bregman, J. N. 1980, ApJ, 236, 577, doi: 10.1086/157776

Cabot, W. H., & Cook, A. W. 2006, NatPh, 2, 562, doi: 10.1038/nphys361

Chandrasekhar, S. 1961, Hydrodynamic and Hydromagnetic Stability (Dover Publications)

Cook, A. W., Cabot, W., & Miller, P. L. 2004, JFM, 511, 333, doi: 10.1017/S0022112004009681

Dalgarno, A., & McCray, R. A. 1972, ARA&A, 10, 375, doi: 10.1146/annurev.aa.10.090172.002111

Dursi, L. J., & Pfrommer, C. 2008, ApJ, 677, 993, doi: 10.1086/529371

Forbes, J. C., & Lin, D. N. C. 2018, arXiv, arXiv:1810.12925. https://arxiv.org/abs/1810.12925

Fraternali, F., Marasco, A., Armillotta, L., & Marinacci, F. 2015, MNRAS, 447, L70, doi: 10.1093/mnrasl/slu182

Heitsch, F., & Putman, M. E. 2009, ApJ, 698, 1485, doi: 10.1088/0004-637X/698/2/1485

Koyama, H., & Inutsuka, S.-I. 2000, ApJ, 532, 980, doi: 10.1086/308594

—. 2002, ApJ, 564, L97, doi: 10.1086/338978

McKee, C. F., & Ostriker, J. P. 1977, ApJ, 218, 148, doi: 10.1086/155667

Oort, J. H. 1966, BAN, 18, 421

—. 1970, A&A, 7, 381

Quilis, V., & Moore, B. 2001, ApJ, 555, L95, doi: 10.1086/322866

Richter, P., de Boer, K. S., Werner, K., & Rauch, T. 2015, A&A, 584, L6, doi: 10.1051/0004-6361/201527451

Roediger, E., & Hensler, G. 2008, A&A, 483, 121, doi: 10.1051/0004-6361:200809438

Ruszkowski, M., Enßlin, T. A., Brüggen, M., Heinz, S., & Pfrommer, C. 2007, MNRAS, 378, 662, doi: 10.1111/j.1365-2966.2007.11801.x

Saul, D. R., Peek, J. E. G., Grcevich, J., et al. 2012, ApJ, 758, 44, doi: 10.1088/0004-637X/758/1/44

Shapiro, P. R., & Field, G. B. 1976, ApJ, 205, 762, doi: 10.1086/154332

Shu, F. H. 1992, Physics of Astrophysics, Vol. II (University Science Books)

Stone, J. M., & Gardiner, T. 2007, ApJ, 671, 1726, doi: 10.1086/523099

Stone, J. M., Gardiner, T. A., Teuben, P., Hawley, J. F., & Simon, J. B. 2008, ApJS, 178, 137, doi: 10.1086/588755

Thom, C., Peek, J. E. G., Putman, M. E., et al. 2008, ApJ, 684, 364, doi: 10.1086/589960

Thom, C., Putman, M. E., Gibson, B. K., et al. 2006, ApJ, 638, L97, doi: 10.1086/501005

Vázquez-Semadeni, E., Gómez, G. C., Jappsen, A. K., et al. 2007, ApJ, 657, 870, doi: 10.1086/510771

Vázquez-Semadeni, E., Ryu, D., Passot, T., González, R. F., & Gazol, A. 2006, ApJ, 643, 245, doi: 10.1086/502710

Vietri, M., Ferrara, A., & Miniati, F. 1997, ApJ, 483, 262, doi: 10.1086/304202

Wakker, B. P. 2001, ApJS, 136, 463, doi: 10.1086/321783

Wakker, B. P., & van Woerden, H. 1997, ARA&A, 35, 217, doi: 10.1146/annurev.astro.35.1.217

Wakker, B. P., York, D. G., Wilhelm, R., et al. 2008, ApJ, 672, 298, doi: 10.1086/523845

Wakker, B. P., York, D. G., Howk, J. C., et al. 2007, ApJ, 670, L113, doi: 10.1086/524222

Wolfire, M. G., Hollenbach, D., McKee, C. F., Tielens, A. G. G. M., & Bakes, E. L. O. 1995, ApJ, 443, 152, doi: 10.1086/175510

Zhou, Y. 2017, PhR, 723-725, 1, doi: 10.1016/j.physrep.2017.07.008